High-resolution, high-contrast mid-infrared imaging of fresh biological samples with ultraviolet-localized photoacoustic microscopy

Junhui Shi[1], **Terence T.W. Wong**[1,2,3], **Yun He**[1,2], **Lei Li**[1], **Ruiying Zhang**[2], **Christopher S. Yung**[4], **Jeeseong Hwang**[4], **Konstantin Maslov**[1], **Lihong V. Wang**[1,*]

[1]Caltech Optical Imaging Laboratory, Andrew and Peggy Cherng Department of Medical Engineering, Department of Electrical Engineering, California Institute of Technology, Pasadena, CA 91125, USA

[2]Optical Imaging Laboratory, Department of Biomedical Engineering, Washington University in St. Louis, St. Louis, MO 63130, USA

[3]Present address: Translational and Advanced Bioimaging Laboratory, Department of Chemical and Biological Engineering, Hong Kong University of Science and Technology, Hong Kong, China

[4]Applied Physics Division, National Institute of Standards and Technology, 325 Broadway Street, Boulder, CO 80305, USA

Abstract

Mid-infrared (MIR) microscopy provides rich chemical and structural information about biological samples, without staining. Conventionally, the long MIR wavelength severely limits the lateral resolution owing to optical diffraction; moreover, the strong MIR absorption of water ubiquitous in fresh biological samples results in high background and low contrast. To overcome these limitations, we propose a method that employs photoacoustic detection highly localized with a pulsed ultraviolet (UV) laser on the basis of the Grüneisen relaxation effect. For cultured cells, our method achieves water-background suppressed MIR imaging of lipids and proteins at UV resolution, at least an order of magnitude finer than the MIR diffraction limits. Label-free histology using this method is also demonstrated in thick brain slices. Our approach provides convenient high-resolution and high-contrast MIR imaging, which can benefit diagnosis of fresh biological samples.

Introduction

As a vibrational imaging modality, mid-infrared (MIR) microscopy has been exploited for applications ranging from material characterization [1–3] to label-free histologic analysis [4–7]. In the last two decades, the sensitivity and speed of MIR microscopy have been significantly improved [8–13], but its biomedical applications still face the following limitations. Conventional transmission MIR microscopy can image only dried or thin samples [1], which requires complicated and time-consuming preparation [6]. In addition, the lateral resolution is diffraction limited to approximately the long MIR wavelength at a typically used numerical aperture (~0.5). Furthermore, for fresh biological samples, the broadband and strong MIR absorption of water creates a huge background, compromising imaging contrast and interfering with molecular analysis.

Many techniques have improved MIR microscopy by addressing one or two of the above limitations. Attenuated total reflection–Fourier transform infrared (ATR-FTIR) microspectroscopic imaging [14,15], a now widely used standard technology, can measure fresh samples in reflection mode with improved spatial resolution, but its penetration depth —due to the use of evanescent waves—is limited to only 1–2 μm. Atomic force microscopy (AFM) has achieved nanoscale resolution by detecting thermal expansion [16–18], light scattering [19], or force [20] induced by MIR laser absorption; however, the surface contact or near-field detection poses challenges in scanning fresh biological samples. Photothermal MIR imaging [21–24], which employs a continuous-wave visible or near-IR laser beam to detect the MIR thermal lensing effect, greatly improves the resolution and somewhat reduces the water background, but the scattering-based detection method restricts its applications to only translucent samples. Stimulated Raman scattering (SRS) imaging has demonstrated label-free chemical mapping of biological cells and tissues at high spatial resolution and contrast [25–27]. Also, far-field super resolution has been achieved using stimulated emission depletion [28,29]. In photoacoustic imaging techniques, although photoacoustic (PA) infrared (PAIR) detection was invented decades ago for spectroscopy and sensing of totally opaque or highly light-scattering materials [30–33], it has only recently been demonstrated to image thick and scattering fresh biological samples without thin slicing [34]. However, it does not address the drawbacks on either spatial resolution or water background.

Here, we present a novel approach, called ultraviolet-localized MIR PA microscopy (ULM-PAM), to achieve high-resolution and nearly water-background–free MIR imaging of fresh biological samples. In our approach, a pulsed mid-MIR laser thermally excites the sample at a focal spot, and a confocal pulsed ultraviolet (UV) laser beam photoacoustically detects the resulting transient temperature rise, thereby reporting the magnitude of the MIR absorption by the sample. This detection scheme is based on the fact that a temperature rise in a sample enhances PA signals, a phenomenon called the Grüneisen relaxation effect [35,36]. While our imaging method reveals MIR absorption contrast, its lateral resolution is determined by the UV wavelength, which is one order of magnitude shorter than the MIR wavelength. In addition, UV light in the range of 200–230 nm is highly absorbed by most biomolecules, such as lipids, proteins, and nucleic acids [37–39], but it is totally transmissive in water [40]. Thus, the strong water background of MIR absorption is suppressed in our method.

Furthermore, the UV light can penetrate up to 100 μm [41], greater than MIR penetration in fresh specimens [23], and the PA signal can propagate in biological tissues with negligible scattering. Therefore, ULM-PAM enables high-resolution and water-background–suppressed PA MIR imaging of fresh thick and scattering biological samples.

Results

PA generation depends on the optical absorption coefficient as well as the pre-laser-pulse temperature. When an object absorbs a short laser pulse, thermal expansion causes it to emit a PA signal. The amplitude of the PA signal is proportional to the absorbed optical energy density, with a coefficient called the Grüneisen parameter (Γ). Γ depends on the volume expansion coefficient and the speed of sound, both of which are temperature-dependent and quasi-linearly proportional to the pre-pulse temperature. As a result, in the physiological temperature range, the Grüneisen parameter depends linearly on the pre-pulse temperature (T), and $\Delta\Gamma/\Gamma \approx 0.04 \cdot \Delta T$ around 20 ˚C for water-rich soft biological tissues [42,43], where Δ denotes small change. Therefore, a pre-pulse temperature rise of 1 degree Celsius can enhance the PA signal by ~4%, and this relationship has been used to photoacoustically measure temperature in tissues [44–46]. When a pulsed laser induces a local transient temperature rise, the local Grüneisen parameter increases within the thermal confinement time (i.e., the time before the local heat diffuses away), which is termed the Grüneisen relaxation effect [35,36]. On this basis, ULM-PAM employs a pulsed UV laser to photoacoustically measure the temperature rise induced by absorption of pulsed MIR laser illumination by the sample.

We realize ULM-PAM using a two-step measurement scheme, as illustrated in Fig. 1a. First, a UV laser pulse generates a baseline PA signal (PA_{UV1}), which is used in conventional UV PA microscopy (UV-PAM) [41,47]. Second, we use dual sequential pulses for MIR heating and UV probing. As soon as an MIR laser pulse heats up the same region, a second UV laser pulse induces another PA signal (PA_{UV2}), where the two laser pulses are separated by a sub-microsecond time interval (Δt) that is shorter than thermal confinement time. In water-rich soft biological tissues, biological molecules are distributed sparsely in the water environment, and the specific heat capacity is approximately homogenous; therefore, the local temperature rise (ΔT) induced by the MIR laser pulse is approximately proportional to the MIR absorption coefficient. Because the local temperature rise increases the local Grüneisen parameter, PA_{UV2} is stronger than PA_{UV1}. The fractional change in PA amplitude, %ΔPA (defined as $\Delta PA / PA_{UV1}$, where $\Delta PA = PA_{UV2} - PA_{UV1}$), is proportional to ΔT, which is proportional to the absorption coefficient at the MIR wavelength. Because the UV wavelength is at least one order of magnitude shorter than the MIR wavelength, the spatial resolution is mainly determined by the focal diameter of the UV laser beam (Fig. 1b). Consequently, the lateral resolution is diffraction limited to λ_{UV}/2NA, where λ_{UV} is the UV wavelength, and NA is the numerical aperture of the objective lens. Because the highest practical NA is approximately 0.5 for both MIR and UV imaging, our approach improves the MIR imaging resolution by at least one order of magnitude from approximately the MIR wavelength to the UV wavelength. In addition, as water has extremely low absorption coefficients (< 0.3 m^{-1}) in the UV region of 200–230 nm (Supplementary Fig. S1), water background from MIR absorption in fresh biological samples is suppressed.

The experimental setup of ULM-PAM is shown in Fig. 1c. The system consists of a pulsed optical parametric oscillator (OPO) MIR (2.5–12.0 μm, 10 ns pulse duration) laser and a pulsed OPO UV laser (210–280 nm, 10 ns pulse duration). The two laser beams are combined by a germanium dichroic mirror and then delivered through an aluminium-coated reflective objective lens (NA = 0.52) to a transmission-mode PA microscopy system. Both the UV and MIR laser beams are focused on the sample, which is mounted on a CaF_2 window attached to the bottom of a water tank. The focal sizes of the UV and MIR are nearly diffraction limited. Configured in transmission mode, an ultrasonic transducer (25 MHz centre frequency) is confocally aligned with the MIR and UV optical foci and collects the PA signals generated by the UV or MIR lasers. The output energy of the UV laser is monitored by a photodiode for pulse-to-pulse calibration of the pulse energy. The time delay between the MIR and UV laser pulses is controlled by a delay generator and set around 100 – 500 ns, which is within the thermal confinement time for hydrated biological samples. The data acquisition, stage scanning, and laser wavelength adjustment are all controlled by a computer. Since the current MIR laser has a pulse repetition rate of up to only 1 kHz, we implement the two-step measurement scheme with two line scans along the *x*-axis instead of one point per step. In two consecutive line scans along the same line, PA_{UV1} with the MIR laser off then PA_{UV2} with the laser on are acquired. In practice, we repeat this two-step scan for each line to improve the signal-to-noise ratio. Once the line scans along each *x*-axis were completed, the sample was step-wise translated along the *y*-axis to form a 2D image.

To characterize our technology using non-biological samples, we first illustrate the ULM-PAM imaging procedure using a 6-μm–diameter carbon fibre on a CaF_2 substrate. This carbon fibre, known to have strong and broadband absorption across the UV to MIR range, was imaged by the ULM-PAM system with a UV wavelength of 266 nm and an MIR wavelength of 3500 nm. For comparison, we also acquired a conventional MIR photoacoustic microscopy (MIR-PAM) image at 3500 nm wavelength. Figure 2a shows the PA amplitude profiles across the carbon fibre. The amplitude profile from conventional MIR-PAM (PA_{MIR}) shows a diffraction-limited low spatial resolution and a high water background as the absorption coefficient of water at 3500 nm is 337.50 cm^{-1} [48]. In ULM-PAM, by contrast, either the UV-PAM amplitude or ΔPA reveals a much sharper boundary of the fibre with lower water background. However, we use %ΔPA to more directly reveal MIR absorption—i.e., to remove the effect of the UV absorption variation. Note that the maximal %PA is ~25%, corresponding to a temperature rise of 7 °C induced by a single MIR laser pulse. This transient temperature rise has been experimentally shown to be safe to live cells [49].

Second, we verified that ULM-PAM is capable of imaging with MIR vibrational absorption contrast. To this end, we measured a ULM-PAM spectrum (Fig. 2b) of a thin layer (~100 μm) of polydimethylsiloxane (PDMS), which has a sharp methyl group absorption line (CH_3) around 3374 nm (2964 cm^{-1}) [50]. The ULM-PAM spectrum was obtained by averaging 100 measurements to reduce noise and was calibrated according to the pulse energy output of the OPO MIR laser. For verification, we also obtained an MIR spectrum of the same PDMS sample with an ATR-FTIR spectrometer as a ground truth. Figure 2b shows good agreement between the ULM-PAM and ATR-FTIR spectra, validating that ULM-PAM can capture MIR-absorption contrast accurately. We focused on the vibrational spectrum of

the methyl groups for demonstration, but ULM-PAM can reveal a variety of chemical bonds at MIR wavelengths in principle, whereas pure UV-PAM without MIR mediation [41,47] reflects electronic absorption at UV wavelengths only.

Third, the spatial resolution of ULM-PAM was quantified to show that MIR imaging with a sub-MIR-diffraction-limited resolution, more than an order of magnitude improvement upon conventional MIR imaging resolution, is possible. To this end, we imaged a 50-nm–diameter carbon nanobead in water at 3500 nm and 224 nm for MIR heating and for UV probing, respectively. The measured full width at half maximum (FWHM) of the single nanobead image from the PA amplitude profile was 260 nm (Fig. 2c), which is close to the theoretical diffraction-limited resolution (250 nm) achievable with the actual 0.45 NA. In conventional MIR PAM, the theoretical diffraction-limited resolution at 3500 nm with the same 0.45 NA objective lens is 3900 nm. One would think single nanobeads may be resolved as long as they are dispersed enough, but their PA signals are actually overwhelmed by the water background, making it difficult to detect. Because the resolution is determined solely by the UV focus, we achieved sub-MIR-diffraction-limited MIR imaging with invariant 260-nm–UV resolution.

Fourth, we further demonstrated the resolution of ULM-PAM by imaging patterns of vertically aligned carbon nanotubes (VACNTs) grown onto a MgF_2 substrate, which was developed as a broad-spectral resolution target for PA imaging [51]. As expected, the conventional MIR-PAM imaging of the patterns (Fig. 2d) suffers from its large diffraction limit, showing only a broad envelope of the carbon-nanotube (CNT) patterns above the water background (Fig. 2f, red dotted line). In comparison, the ULM-PAM image (Fig. 2e) reveals rich details of the VACNT patterns. Although the VACNTs within the patterns are of the same length, VACNT density across the pattern may not be uniform due to nonuniform distribution of the CVD growing catalysts on the MgF_2 substrate, and the ULM-PAM in fact reveals PA amplitude variations within the pattern. Moreover, ULM-PAM detects even finer features, such as satellite rings around the pattern (see the image in Fig. 2e, and the amplitude profile across the pattern in Fig. 2f, blue solid line), which may be originated from optical lithography artefacts when using a transparent MgF_2 substrate with a direct laser write photography technique (See supplementary Fig. S2 of confocal backscatter microscopy and transmission optical microscopy images of a VACNT sample from the same batch). The 400-nm FWHM of the satellite rings (see the inset in Fig. 2f) is comparable to the wavelength of the laser (405 nm) used for direct write lithography.

To demonstrate ULM-PAM's capability of subcellular molecular imaging, we prepared freshly formalin-fixed 3T3 mouse fibroblast cells for mapping the distribution of intracellular lipids and proteins. We tuned the UV wavelength to 224 nm, where almost all proteins, lipids, and nucleic acids have strong absorption with molar absorption coefficients on the order of 10^4 $M^{-1}cm^{-1}$ for proteins and 10^6 $M^{-1}cm^{-1}$ for nucleic acids [52]. For lipid imaging, we set the MIR wavelength to the absorption peak at 3420 nm (2924 cm^{-1}), corresponding to the asymmetric stretching mode of the CH_2 group—the dominant constituent of lipids [6]. The ULM-PAM for lipids resolved many small aggregated globules (Fig. 3a), attributed to rich oleic acid molecules in the droplets. For protein imaging, we used 6050 nm (1653 cm^{-1}) to target the amide I band—the most absorptive one in proteins.

As shown in Fig. 3b, the signals are scant in the nucleic region and abundant in other regions due to the reduced cytoplasm thickness above, confirming that they are from intracellular organelles. Their tubular or vesicular forms with gradually decreasing density from the middle to the cell edge indicates that they are protein containing organelles such as endoplasmic reticulum, Golgi apparatus, and secretory vesicles. Furthermore, the filamentous structures near the cell edge are resolved and are likely cytoskeletons in fibroblast cells. To our knowledge, it is the first time that MIR microscopy reveals the sub-cellular protein distribution in hydrated cells at such a fine resolution. To complete high resolution and high contrast chemical mapping of major intracellular biomolecules, including nucleic acids, we used a 250 nm UV wavelength to directly generate a UV-PAM image (Fig. 3c), based on the strong electronic absorption of nucleic acids [39,47]. The image with strong signals from the cell nuclei resolves details of the sub-nucleic distribution of nucleic acids. For this nucleic acid imaging, MIR lasers were not used, since the DNA/RNA is partially invisible in MIR imaging, mainly owing to its band overlap with other chemical bonds and low MIR absorption [53,54]. The spatial resolution and image contrast stand out in comparison with the conventional MIR-PAM images of lipids (Fig. 3d) and proteins (Fig. 3e), obtained at 3420 nm and 6050 nm, respectively, displaying poor spatial resolution and strong water background. For quantitative assessment, four amplitude profiles across the same line in Fig. 3a, 3b, 3d, and 3e are compared in Fig. 3f. The ULM-PAM images reveal many fine features, while the regular MIR-PAM images do not because of the resolution limit. Overlaying the individual images of lipids, proteins, and nucleic acids shown in Figs. 3a–3c constructs a complete molecular map of a fibroblast cell without labelling (Fig. 3g). This advantage allows us to study cellular metabolisms and activities at different stages. As a demonstration, the images of mature (Fig. 3h) and neonatal (Fig. 3i) cells are compared. On the one hand, a broader spatial distribution of proteins and more filamentous structures in the neonatal cells imply that the neonatal cells may have more active protein metabolism and higher mobility involving more actin fibres. On the other hand, the mature cell contains more lipid droplets not associated with proteins, indicative of less metabolic activity.

Another important application of ULM-PAM is label-free PA histology of thick tissue slices. Since the study of nerve fibres is important in brain science, and myelin is one of the main chemical components of axons in the central nervous system, we implemented ULM-PAM to study the structural details of cerebrum and cerebellum in a mouse brain *ex vivo*. A microtome sliced a coronal cerebrum section and a horizontal cerebellum section, both 300 μm thick, from a freshly formalin-fixed mouse brain. Initially, myelin images of these two sections (Figs. 4a and 4b) in fully hydrated state were acquired by MIR-PAM at 3420 nm, which is the peak absorption wavelength of myelin lipids. The MIR-PAM images of the cerebrum and cerebellum sections are both similar to histology or dyed-stained fluorescence images, exhibiting rich structural information of nerve fibres or fibre bundles. However, in low spatial resolution and low contrast MIR-PAM images, finer details such as concentration gradient and structural details across the boundary between the retrosplenial cortex and grey cortical region are hardly resolved.

To reveal the finer details, we used ULM-PAM, with a UV wavelength of 224 nm and an MIR wavelength of 3420 nm, to achieve higher-resolution and water-background–free MIR imaging of myelin in the tissue. We first used MIR-PAM to scan a small area of interest

(Fig. 4c), which corresponds to the retrosplenial cortex in the cerebrum (region I in Fig. 4a), and then used ULM-PAM to image the same area (Fig. 4d) for comparison. The ULM-PAM clearly resolves fine structures of nerve fibres or bundles in the retrosplenial cortical region. We further overlaid the ULM-PAM image of myelin with an UV-PAM image of nucleic acids acquired at 250 nm (Supplementary Fig. S3), yielding a histology-like image (Fig. 4e). We call this method 'PA histology', showing both myelin (green) and nucleic acid (purple) distributions. To validate the PA-histology image, the same brain slice was further sectioned into thinner slices, stained by myelin axon-specific Luxol fast blue (LFB), and imaged by conventional optical microscopy (Fig. 4f). The PA-histologic image (Fig. 4e) and the LFB-stained image (Fig. 4f) show the same details with concentrated myelin distributions in the RC (bright green in the PA-histology and bright blue in the LFB-stain histology) and punctate pattern indicative of cell nuclei (purple in the PA-histology and punctate dark blue in the LFB-stain histology). In addition, we performed the same experiment on another region (region II in Fig. 4b) of the cerebellum section. The resulting ULM-PAM image (Fig. 4h) shows dense nerve bundles in the arbor vitae region and sparse but clear nerve fibres radiating into the granular region, whereas the PA-histologic image (Fig. 4i) reveals the densely distributed nucleic acids of non-myelinated cells in the granular region. The LFB-stained image (Fig. 4j) also validates the PA-histologic image of region II in the cerebellum section. These results demonstrate that ULM-PAM is capable of imaging myelin distribution and revealing nerve fibres or bundles in thick brain slices at high resolution and low water background without any exogenous labels. Further, aided with UV-PAM imaging of nucleic acids, it can generate PA-histologic images that are similar to standard LFB-stained histologic images.

Discussion

ULM-PAM is a novel high-resolution and water-background–suppressed MIR microscopy modality capable of imaging fresh biological samples without staining. For cells, ULM-PAM provides sub-cellular MIR imaging of lipids and proteins with high contrast without the highly obscuring water background. For tissue slices, ULM-PAM produces label-free PA-histologic images without requiring thinly slicing and drying samples, unlike conventional MIR imaging [6]. At the MIR wavelength of 3420 nm—targeting CH_2 stretching, water absorbs less than the molecules of interest, and at the UV wavelength, water is almost transparent; therefore, ULM-PAM eliminates water background nearly completely. At the MIR wavelengths where water absorbs more than the molecules of interest, e.g. the amide A band around 3000 nm, neighbouring water within the thermal diffusion range may interfere with the temperature rise of the targeted molecules. However, by shortening the time delay between the MIR and UV pulses [55], the thermal diffusion length can be reduced to <50 nm, far less than the UV focal diameter. Consequently, the effect of neighbouring water is substantially suppressed. Our initial system can be extended to cover the full MIR spectral range, allowing exploration of many more molecules of interest. To our knowledge, among the existing far-field MIR imaging approaches, ULM-PAM has achieved the highest imaging resolution at 250 nm, which can be further improved by using a higher-NA objective lens and a shorter UV wavelength. In addition, ULM-PAM

can potentially bridge the resolution gap from 100 nm to 400 nm between AFM-MIR and other MIR imaging modalities, such as ATR-FTIR and photothermal MIR.

Currently, ULM-PAM still faces some technical limitations. First, although raw PA amplitudes have high signal-to-noise ratios, their fractional changes are noisy mainly because two successive UV laser pulses are non-identical. Our current UV laser has ~25% energy fluctuation at 224 nm with additional mode hopping, which cannot be easily corrected for by photodiode calibration. A more stable UV laser would greatly benefit ULM-PAM. Alternatively, a long optical fibre delay line can be employed to replicate the UV pulse with a preset time delay to avoid inter-pulse fluctuation. In addition, the pulse energy of our current MIR laser in the fingerprint region (> 6600 nm) fluctuates so prominently that ULM-PAM could not be realized stably. Second, the imaging speed is restricted by the pulse repetition rates of the lasers, currently only up to 1 kHz, which is inadequate for real-time imaging. For example, it takes more than two hours to scan a 1 mm × 1 mm area with a 500 nm step size, and usually more than ten scans are needed for averaging, to compensate for the inter-pulse fluctuation. If the pulse repetition rate reaches 200 kHz and the pulse energy is sufficiently stable, the imaging time without averaging can be reduced by 200 times to about 40 s. Furthermore, multi-focal PA imaging using a linear array of ultrasonic transducers can improve the imaging speed dramatically, typically more than 100 times [56,57]. Therefore, the acquisition time can potentially be shortened to 0.4 s, enabling *in vivo* imaging. ULM-PAM can also explore the fingerprint region to yield rich vibration information. Third, our current transmission-mode system cannot be switched to reflection mode because an MIR-transparent coupling medium with low acoustic attenuation has not been found. To realize reflection mode, surface-wave acoustic detection may be employed. Fourth, depth cannot be optically resolved in the current system. Because the focal zone of the MIR laser is much longer than that of the UV laser, the axial resolution is the same as that of conventional UV-PAM, which lacks optical sectioning capability. A cross-beam configuration, in which the MIR and UV laser beams cross at an angle while confocally targeting at the same object, may improve the axial resolution.

Thus far, two vibrational imaging microscopies provide far-field and label-free imaging at sub-cellular resolution: Raman scattering microscopy [58,59] and photothermal MIR microscopy [21,23]. First, compared with Raman scattering microscopy, ULM-PAM—leveraging direct MIR photon absorption—is of higher sensitivity, since the fundamental MIR cross-section is several orders of magnitude greater than that of the Raman scattering cross-section [7]. Second, ULM-PAM not only exhibits the same features as Raman scattering microscopy, such as low water background, but can also be extended to direct imaging of various vibrational bonds that are not Raman-active in the wide mid-MIR spectral range [23]. Third, ULM-PAM provides a higher spatial resolution due to the short UV wavelength. Compared with photothermal MIR microscopy, our method is essentially a new way to exploit the MIR photothermal effect, but we use PA detection instead to retrieve the MIR-absorption induced local temperature rise, enabling MIR imaging in thick, highly optically absorbing and scattering biological samples. More importantly, PA temperature sensing is based on the Grüneisen relaxation effect, which gives a PA signal change of about 3%/ºC in the physiological temperature range. This change is two orders of magnitude greater than the photothermally induced refractive index change (~10^{-4}/ºC), making ULM-PAM more

sensitive than photothermal MIR microscopy. In this work, ULM-PAM imaged a 50-nm bead in water (see Fig. 2(c)) with a signal-to-noise ratio of about 7, while the total data acquisition time was only about 1 μs for each pixel, outperforming the current photothermal MIR microscopy based on lock-in detection [23,24]. Furthermore, since water is almost transparent at UV wavelengths from 200 nm to 230 nm, the water background of MIR imaging is suppressed in ULM-PAM. Finally, the shorter UV wavelength endows our method with higher resolution than photothermal MIR imaging, which is based on visible or near-infrared light detection.

Our method can be further developed to attain nanoscale far-field chemical imaging by extending the wavelength of the probe beam to the X-ray regime. Current X-ray microscopy for biological samples operates either in the soft X-ray regime for water transparency (2.33–4.40 nm) or the hard X-ray regime [60,61], using imaging contrast arising from natural X-ray absorption, to provide nanometre scale resolution. Imaging specific chemicals or structures inside biological samples requires exogenous labelling, *e.g.*, silver-enhanced immunogold labelling [62]. Interestingly, X-ray acoustic imaging has also been demonstrated with a pulsed X-ray source [63]. By combining the MIR-absorption induced Grüneisen relaxation effect and X-ray-acoustic imaging, we can expect to achieve X-ray-acoustic imaging with MIR-absorption contrast, utilizing acoustic signals generated by pulsed X-rays to report MIR absorption contrast in materials, thereby achieving far-field and label-free imaging at nanometre scale resolution.

Methods

System configuration.

We used an OPO mid-MIR laser (NT242-SH, EKSPLA) and an OPO UV laser (NT270, EKSPLA). The wavelength of the OPO mid-MIR laser is tunable from 2.5 to 12 μm (from 4000 to 833 cm–1), its pulse duration is about 10 ns, and the output pulse energy varies from 10 to 100 μJ depending on the selected wavelength. Both lasers have a pulse repetition rate of up to 1 kHz. The two lasers are synchronized with external triggers—controlling the delay between the UV and MIR laser pulses. For imaging lipids and proteins using ULM-PAM, the UV laser was tuned to 224 nm; for imaging nucleic acids using UV-PAM, it was set to 250 nm. Both the MIR and UV beams, with diameters of about 4 mm, were reflected by several UV-enhanced aluminium coated mirrors (PF10–03-F01, Thorlabs), and focused to a sample mounted on a CaF_2 window through a 36X reflective objective lens (50102–02, Newport, 0.52 NA). PA signals were detected in transmission mode by a focused ultrasonic transducer (25 MHz centre frequency, V324-SM, Olympus), which has an acoustic focal length of 12.7 mm and an element diameter of 6 mm. The acoustic coupling medium was de-ionized water. PA signals were amplified by ~50 dB using two low-noise amplifiers (ZFL-500LN+, Mini-circuits), and then acquired by a DAQ card (Razor 14, Gage) at 14 bits and 200 MS/s.

Raster scanning for images.

ULM-PAM images of the sample at selected wavelengths were obtained by raster scanning using two motorized stages (PLS-85, PI miCos) coupled to the sample holder. To drive the

scanning stages at high precision (50 nm step size) with minimal low-frequency vibration, we used two five-phase stepper motors (PKP546MN18B, Oriental Motor) and the associated drivers (CVD518-K, Oriental Motor). Line scans along the *x*-axis were averaged to compensate for UV laser inter-pulse fluctuation. The laser tuning, data acquisition, and scanning systems were synchronized by a central computer via micro-controllers, using LabVIEW. The scan step size varied for different samples. The point spread function of a 50-nm–diameter carbon nanobead was measured using a 50 nm step size. Imaging cells was done with a 200 nm step size. For imaging brain slices, to compensate for the slow laser repetition rates of the lasers, we shrank the UV beam to reduce the effective NA to 0.16, which worsened the resolution to some extent, but accelerated the scanning with a larger step size (500 nm) and effectively extended the focal depth to accommodate uneven sample surfaces.

ATR-FTIR measurements.

All ATR-FTIR spectra were measured on an ATR-FTIR spectrometer (Nicolet 6700, Thermo) in the Molecular Materials Research Center at California Institute of Technology. The baseline was calibrated by measuring a blank sample.

Spatial resolution measurement. Carbon nanoparticles (~50 nm diameter; US1074, US Research Nanomaterials) were sparsely distributed on the surface of a CaF_2 window. A layer of low-gelling-temperature agarose (A9414–100G, Sigma-Aldrich) was placed on top of the window to fix the nanoparticles. The sample was imaged in 50 nm steps.

Cell culture preparation.

Mouse embryonic fibroblast cells (3T3-L1) were obtained from American Type Culture Collection (ATCC). The cells were seeded onto 1-mm–thick CaF_2 substrates, and then maintained at 37 °C and 5% CO2 in Dulbecco's modified Eagle's medium (DMEM, Sigma Aldrich) supplemented with 10% bovine calf serum (Sigma Aldrich). When the cells were ~100% confluent, in order to induce some cells to form oleic acid droplets, the medium was changed to the adipocyte differentiation medium containing 90% DMEM, 10% fetal bovine serum (FBS), 1.0 μM dexamethasone, 0.5 mM isobutylmethylxanthine and 1.0 μg/mL insulin, all from Sigma Aldrich. Two days later, the medium was changed to adipocyte maintenance medium (90% DMEM, 10% FBS and 1.0 μg/mL insulin), and incubated for another two days. Finally, partially differentiated cells were fixed in 3.7% formalin solution, and washed with phosphate buffered saline.

Tissue slice preparation.

The brain was extracted from Swiss Webster mice (Hsd: ND4, Harlan Laboratories), and fixed in 3.7% formalin solution at room temperature. Afterwards, the fixed brain was embedded in 4% agarose and then sectioned by a microtome (VT1200 S, Leica) into slices 300 μm thick. All experimental animal procedures were carried out in conformity with a laboratory animal protocol approved by the Animal Studies Committee of California Institute of Technology. After they are imaged by ULM-PAM, the thick slices underwent standard procedures for histological staining (including paraffinization, slicing into 10 μm in thickness, and staining), and were finally imaged in a digital pathology system (VENTANA

iScan HT, Roche). It should be noted that some samples were fragmented and slightly distorted during the thin-slicing procedure, which did not affect the comparison. The whole LFB-stained-histologic image of the cerebrum and cerebellum is shown in Supplementary Fig. S4.

Data analysis.

Raw PA data for each pixel were acquired within a time window of 0.5 μs for one laser shot. For calibration, each UV PA signal was divided by the maximal value of the photodiode signal pulse by pulse. PA signals were band-pass filtered to remove noise outside the transducer's bandwidth. The difference signal $\Delta PA = PAUV2 - PAUV1$ was calculated in the time domain, and its maximum amplitude projection (MAP) was computed to construct an image. The fractional change in PA amplitude was computed by $\%\Delta PA = \Delta PA / (PAUV1 + \lambda)$, where λ was chosen as several times of the root-mean-square noise level. This technique is similar to the Tikhonov regularization. The final images were further processed with a median filter to reduce salt-and-pepper noise.

Supplementary Material

Refer to Web version on PubMed Central for supplementary material.

Acknowledgements

References

1. Wetzel DL & LeVine SM Imaging molecular chemistry with infrared microscopy. Science 285, 1224–5 (1999). [PubMed: 10484732]

2. Koenig JL Microspectroscopic imaging of polymers. (American Chemical Society, 1998).

3. Prati S, Joseph E, Sciutto G & Mazzeo R New advances in the application of FTIR microscopy and spectroscopy for the characterization of artistic materials. Acc. Chem. Res 43, 792–801 (2010). [PubMed: 20476733]

4. Diem M, Romeo M, Boydston-White S, Miljkovic M & Matthaus C A decade of vibrational micro-spectroscopy of human cells and tissue (1994–2004). Analyst 129, 880–5 (2004). [PubMed: 15457314]

5. Fernandez DC, Bhargava R, Hewitt SM & Levin IW Infrared spectroscopic imaging for histopathologic recognition. Nat. Biotechnol 23, 469–474 (2005). [PubMed: 15793574]

6. Baker MJ et al. Using Fourier transform IR spectroscopy to analyze biological materials. Nat. Protoc 9, 1771–1791 (2014). [PubMed: 24992094]

7. Diem M et al. Molecular pathology via IR and Raman spectral imaging. J. Biophotonics 6, 855–886 (2013). [PubMed: 24311233]

8. Griffiths P Fourier transform infrared spectrometry. Science 21, 297–302 (1983).

9. Lewis EN et al. Fourier transform spectroscopic imaging using an infrared focal-Plane array detector. Anal. Chem 67, 3377–3381 (1995). [PubMed: 8686889]

10. Miller LM, Smith GD & Carr GL Synchrotron-based biological microspectroscopy: From the mid-infrared through the far-infrared regimes. J. Biol. Phys 29, 219–230 (2003). [PubMed: 23345838]

11. Nasse MJ et al. High-resolution Fourier-transform infrared chemical imaging with multiple synchrotron beams. Nat. Methods 8, 413–416 (2011). [PubMed: 21423192]

12. Kole MR, Reddy RK, Schulmerich MV, Gelber MK & Bhargava R Discrete frequency infrared microspectroscopy and imaging with a tunable quantum cascade laser. Anal. Chem 84, 10366–10372 (2012). [PubMed: 23113653]

13. Haas J & Mizaikoff B Advances in mid-infrared spectroscopy for chemical analysis. Annu. Rev. Anal. Chem 9, 45–68 (2016).

14. Sommer AJ, Marcott C, Story GM & Tisinger LG Attenuated total internal reflection infrared mapping microspectroscopy using an imaging microscope. Appl. Spectrosc Vol. 55, Issue 3, pp. 252–256 55, 252–256 (2001).

15. Chan KLA & Kazarian SG New opportunities in micro- and macro-attenuated total reflection infrared spectroscopic imaging: spatial resolution and sampling versatility. Appl. Spectrosc 57, 381–389 (2003). [PubMed: 14658633]

16. Dazzi A, Prazeres R, Glotin F & Ortega JM Local infrared microspectroscopy with subwavelength spatial resolution with an atomic force microscope tip used as a photothermal sensor. Opt. Lett 30, 2388 (2005). [PubMed: 16196328]

17. Lu F, Jin M & Belkin MA Tip-enhanced infrared nanospectroscopy via molecular expansion force detection. Nat. Photonics 8, 307–312 (2014).

18. Dazzi A & Prater CB AFM-IR: technology and applications in nanoscale infrared spectroscopy and chemical imaging. Chem. Rev 117, 5146–5173 (2017). [PubMed: 27958707]

19. Knoll B & Keilmann F Near-field probing of vibrational absorption for chemical microscopy. Nature 399, 134–137 (1999).

20. Nowak D et al. Nanoscale chemical imaging by photoinduced force microscopy. Sci. Adv 2, e1501571–e1501571 (2016). [PubMed: 27051870]

21. Furstenberg R, Kendziora CA, Papantonakis MR, Nguyen V & McGill RA Chemical imaging using infrared photothermal microspectroscopy. in Proceedings of SPIE Defense, Security, and Sensing (eds. Druy MA & Crocombe RA) 837411 (2012).

22. Li Z, Kuno M & Hartland G Super-resolution imaging with mid-IR photothermal microscopy on the single particle level in Proceedings of SPIE Physical Chemistry of Interfaces and Nano-materials XIV (eds. Hayes SC & Bittner ER) 9549, 954912 (International Society for Optics and Photonics, 2015).

23. Zhang D et al. Depth-resolved mid-infrared photothermal imaging of living cells and organisms with submicrometer spatial resolution. Sci. Adv 2, e1600521 (2016). [PubMed: 27704043]

24. Li Z, Aleshire K, Kuno M & Hartland GV Super-resolution far-field infrared imaging by photothermal heterodyne imaging. J. Phys. Chem. B 121, 8838–8846 (2017). [PubMed: 28741348]

25. Lu F-K et al. Label-free DNA imaging in vivo with stimulated Raman scattering microscopy. Proc. Natl. Acad. Sci. U. S. A 112, 11624–9 (2015). [PubMed: 26324899]

26. Cheng J-X & Xie XS Vibrational spectroscopic imaging of living systems: An emerging platform for biology and medicine. Science (80-.). 350, aaa8870–aaa8870 (2015).

27. Ji M et al. Detection of human brain tumor infiltration with quantitative stimulated Raman scattering microscopy. Sci. Transl. Med 7, 309ra163 (2015).

28. Gong L & Wang H Breaking the diffraction limit by saturation in stimulated-Raman-scattering microscopy: A theoretical study. Phys. Rev. A 90, 13818 (2014).

29. Silva WR, Graefe CT & Frontiera RR Toward Label-Free Super-Resolution Microscopy. ACS Photonics (2016).

30. Rockley MG Fourier-transformed infrared photoacoustic spectroscopy of polystyrene film. Chem. Phys. Lett 68, 455–456 (1979).

31. Patel CKN & Tam AC Pulsed optoacoustic spectroscopy of condensed matter. Rev. Mod. Phys 53, 517–550 (1981).

32. Tam AC Applications of photoacoustic sensing techniques. Rev. Mod. Phys 58, 381–431 (1986).

33. Michaelian KH Photoacoustic infrared spectroscopy. (John Wiley & Sons, Inc., 2003).

34. Sim JY, Ahn C-G, Jeong E-J & Kim BK In vivo microscopic photoacoustic spectroscopy for non-invasive glucose monitoring invulnerable to skin secretion products. Sci. Rep 8, 1059 (2018). [PubMed: 29348411]

35. Wang L, Zhang C & Wang LV Grueneisen relaxation photoacoustic microscopy. Phys. Rev. Lett 113, 174301 (2014). [PubMed: 25379919]

36. Lai P, Wang L, Tay JW & Wang LV Photoacoustically guided wavefront shaping for enhanced optical focusing in scattering media. Nat. Photonics 9, 126–132 (2015). [PubMed: 25914725]

37. Kunitz M Crystalline desoxyribonuclease; isolation and general properties; spectrophotometric method for the measurement of desoxyribonuclease activity. J. Gen. Physiol 33, 349–62 (1950). [PubMed: 15406373]

38. Beaven GH & Holiday ER Ultraviolet absorption spectra of proteins and amino acids. Adv. Protein Chem 7, 319–386 (1952). [PubMed: 14933256]

39. Yao D-K, Maslov KI, Wang LV, Chen R & Zhou Q Optimal ultraviolet wavelength for in vivo photoacoustic imaging of cell nuclei. J. Biomed. Opt 17, 056004 (2012). [PubMed: 22612127]

40. Quickenden TI & Irvin JA The ultraviolet absorption spectrum of liquid water. J. Chem. Phys 72, 4416–4428 (1980).

41. Wong TTW et al. Fast label-free multilayered histology-like imaging of human breast cancer by photoacoustic microscopy. Sci. Adv 3, e1602168 (2017). [PubMed: 28560329]

42. Danielli A et al. Label-free photoacoustic nanoscopy. J. Biomed. Opt 19, 086006 (2014). [PubMed: 25104412]

43. Xu S, Scherer GW, Mahadevan TS & Garofalini SH Thermal Expansion of Confined Water. Langmuir 25, 5076–5083 (2009). [PubMed: 19275191]

44. Larina IV, Larin KV & Esenaliev RO Real-time optoacoustic monitoring of temperature in tissues. J. Phys. D. Appl. Phys 38, 2633–2639 (2005).

45. Shah J et al. Photoacoustic imaging and temperature measurement for photothermal cancer therapy. J. Biomed. Opt 13, 034024 (2008). [PubMed: 18601569]

46. Yao J, Ke H, Tai S, Zhou Y & Wang LV Absolute photoacoustic thermometry in deep tissue. Opt. Lett 38, 5228 (2013). [PubMed: 24322224]

47. Yao D-K, Maslov K, Shung KK, Zhou Q & Wang LV In vivo label-free photoacoustic microscopy of cell nuclei by excitation of DNA and RNA. Opt. Lett 35, 4139 (2010). [PubMed: 21165116]

48. Hale GM & Querry MR Optical Constants of Water in the 200-nm to 200-μm Wavelength Region. Appl. Opt 12, 555 (1973). [PubMed: 20125343]

49. Simanovskii DM et al. Cellular tolerance to pulsed hyperthermia. Phys. Rev. E 74, 011915 (2006).

50. Mata A, Fleischman AJ & Roy S Characterization of polydimethylsiloxane (PDMS) properties for biomedical micro/nanosystems. Biomed. Microdevices 7, 281–293 (2005). [PubMed: 16404506]

51. Hwang J. SPIE Photonics West. Development of photoacoustic phantoms towards quantitative evaluation of photoacoustic imaging devices. SPIE Photonics West 10494–77; 2018.

52. Schmid F-X Biological macromolecules: UV-visible spectrophotometry in Encyclopedia of life sciences (Macmillan Publishing Group, 2001).

53. Lasch P, Boese M, Pacifico A & Diem M FT-IR spectroscopic investigations of single cells on the subcellular level. Vib. Spectrosc 28, 147–157 (2002).

54. Wood BR The importance of hydration and DNA conformation in interpreting infrared spectra of cells and tissues. Chem. Soc. Rev 45, 1980–1998 (2016). [PubMed: 26403652]

55. Wang LV & Wu H Biomedical optics: principles and imaging. (Wiley-Interscience, 2007).

56. Song L, Maslov K & Wang LV Multifocal optical-resolution photoacoustic microscopy in vivo. Opt. Lett 36, 1236 (2011). [PubMed: 21479041]

57. Imai T et al. High-throughput ultraviolet photoacoustic microscopy with multifocal excitation. J. Biomed. Opt 23, 1 (2018).

58. Evans CL & Xie XS Coherent anti-stokes Raman scattering microscopy: chemical imaging for biology and medicine. Annu. Rev. Anal. Chem 1, 883–909 (2008).

59. Zhang C, Zhang D & Cheng J-X Coherent Raman scattering microscopy in biology and medicine. Annu. Rev. Biomed. Eng 17, 415–445 (2015). [PubMed: 26514285]

60. Sakdinawat A & Attwood D Nanoscale X-ray imaging. Nat. Photonics 4, 840–848 (2010).

61. Berglund M, Rymell L, Peuker M, Wilhein T & Hertz HM Compact water-window transmission X-ray microscopy. J. Microsc 197, 268–273 (2000). [PubMed: 10692130]

62. Meyer-Ilse W et al. High resolution protein localization using soft X-ray microscopy. J. Microsc 201, 395–403 (2001). [PubMed: 11240856]

63. Xiang L, Tang S, Ahmad M & Xing L High resolution X-ray-induced acoustic tomography. Sci. Rep 6, 26118 (2016). [PubMed: 27189746]
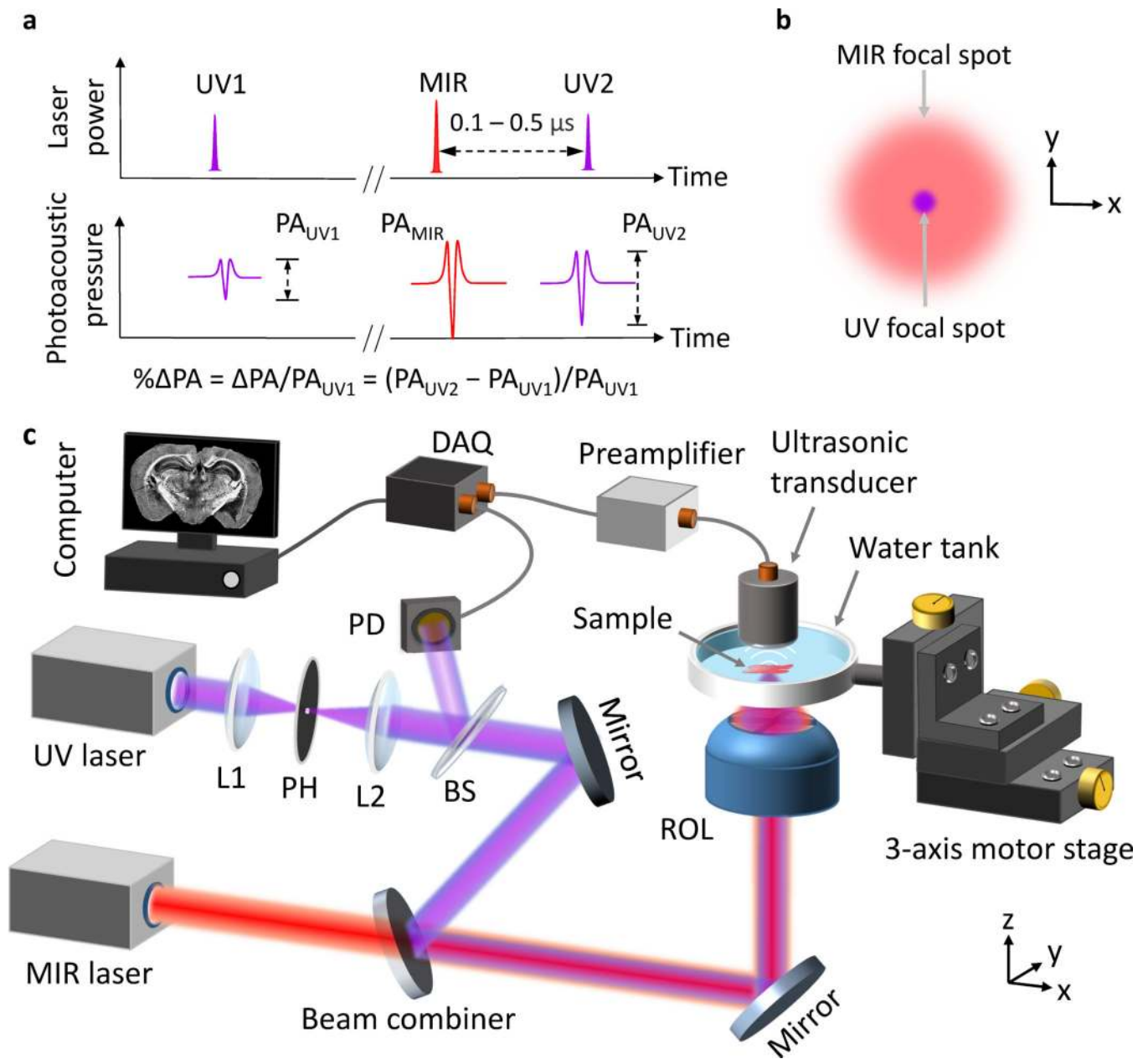
Figure 1.
Ultraviolet-localized mid-infrared (MIR) photoacoustic (PA) microscopy (ULM-PAM). a. Principle of ULM-PAM. Two ultraviolet (UV) laser pulses generate PA signals PA_{UV2} and PA_{UV1} before and after an MIR laser excitation. Because the MIR absorption increases the Grüneisen parameter, PA_{UV2} is greater than PA_{UV1}; thus, $\%\Delta PA$ reveals the MIR absorption. b. Confocal illumination areas of the MIR and UV laser beams on the focal plane. c. Schematic of the experimental setup. The UV and MIR laser beams are confocally delivered to the sample in a transmission-mode PA microscope. BS, beam splitter; DAQ, data acquisition unit; L1, L2, lenses; PD, photodiode; PH, pinhole; ROL, reflective objective lens consisting of a convex followed by a concave mirror (details not shown). The electronic

connections for controls are not shown. The data acquisition speed is limited by the pulse repetition rate of the MIR laser, which is 1 kHz.
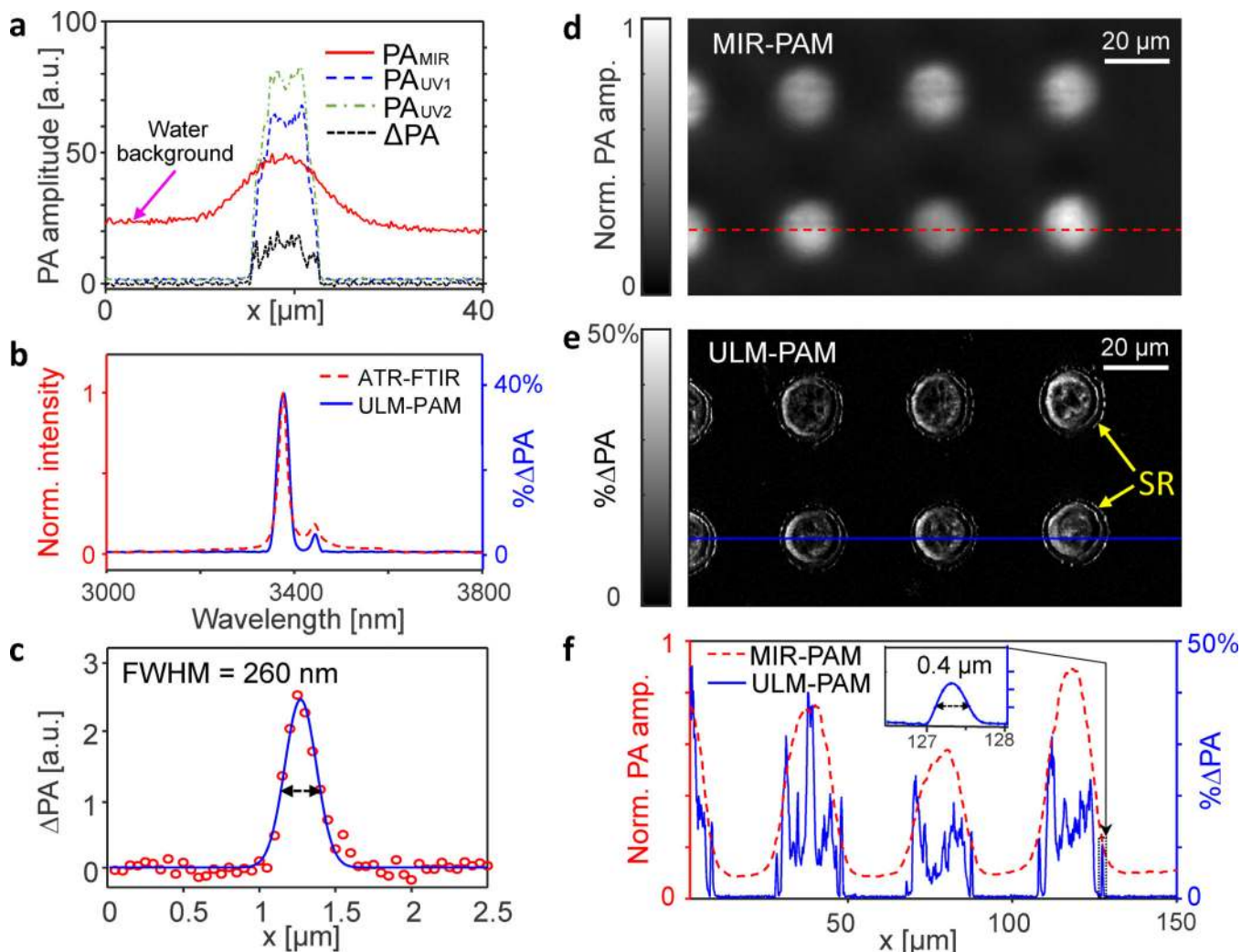
Figure 2.
System characterization. a. Cross-sectional line images of a 6-μm–diameter carbon fibre. The MIR-PAM image (PA_{MIR}) has a low resolution and a high water background, while the differential image ΔPA has a much sharper edge and lower water background. b. Comparison of the ULM-PAM and ATR-FTIR spectra of a thin layer of PDMS. c. Effective point spread function of ULM-PAM, measured using a 50-nm–diameter carbon nanobead. d, e. Comparison of MIR-PAM (d) and ULM-PAM (e) images of a VACNT pattern on a MgF_2 substrate. SR, satellite rings. f. Amplitude profiles along the dashed lines in d and e showing that MIR-PAM depicts only the envelopes of the VACNT pattern while ULM-PAM shows crisp cross-sectional structures and even 400-nm fine features.
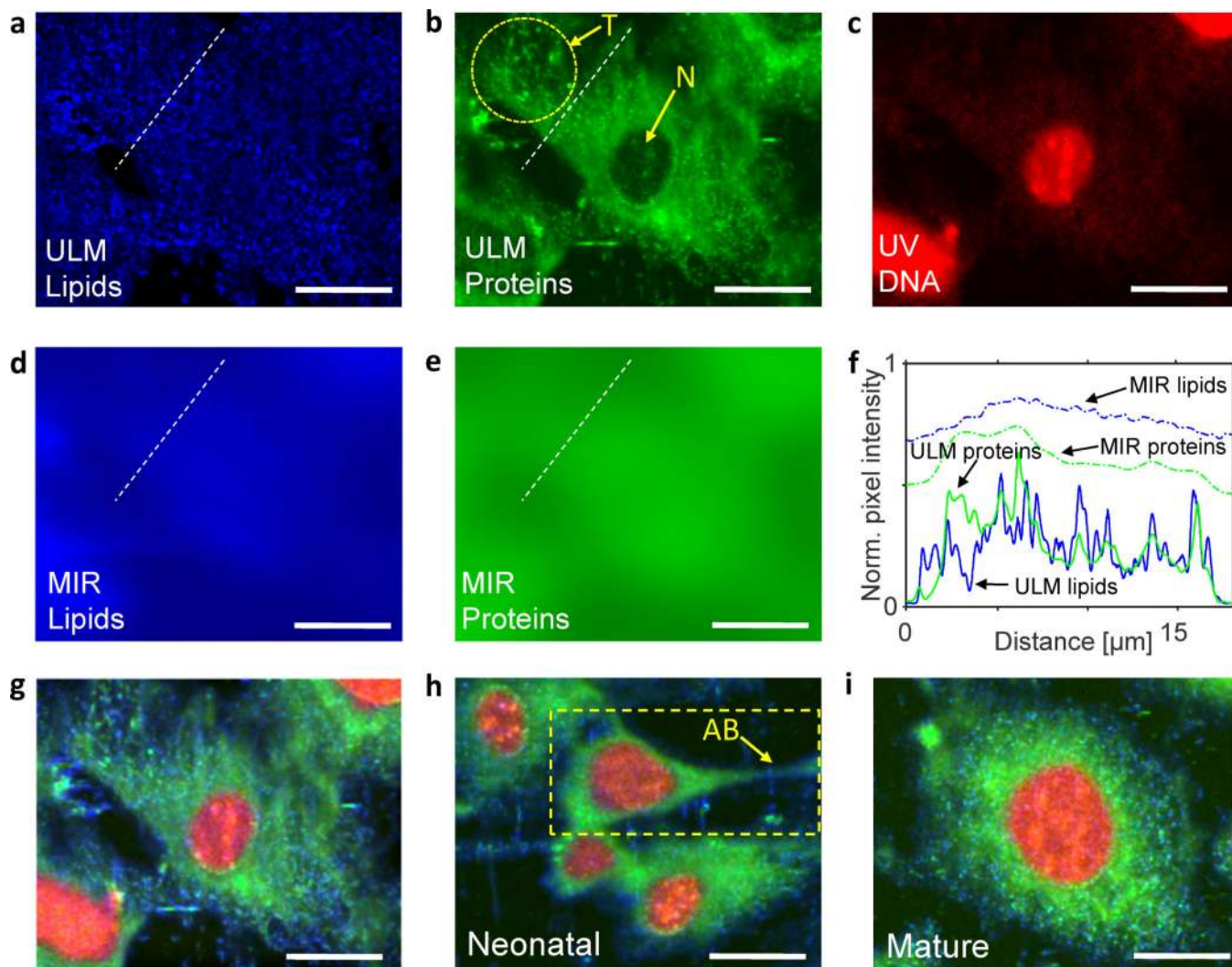
Figure 3.
Imaging of lipids, proteins, and nucleic acids in fibroblast cells. a, b. ULM-PAM images of (a) lipids and (b) proteins. T, tubular structures; N, nucleic region. c. UV-PAM image of nucleic acids. d, e. MIR-PAM images of (d) lipids and (e) proteins, imaged at 3420 nm and 6050 nm, respectively. f. Comparison of line profiles along the dashed lines in the ULM-PAM lipid (a), ULM-PAM protein (b), MIR-PAM lipid (d), and MIR-PAM protein (e) images. g. Composite image of a cell formed by overlaying the images of (a) lipids, (b) proteins, and (c) nucleic acids in different colour channels. h, i. Composite images of the cells at (h) neonatal and (i) mature stages. AB, actin bundles. Scale bars, 10 μm.
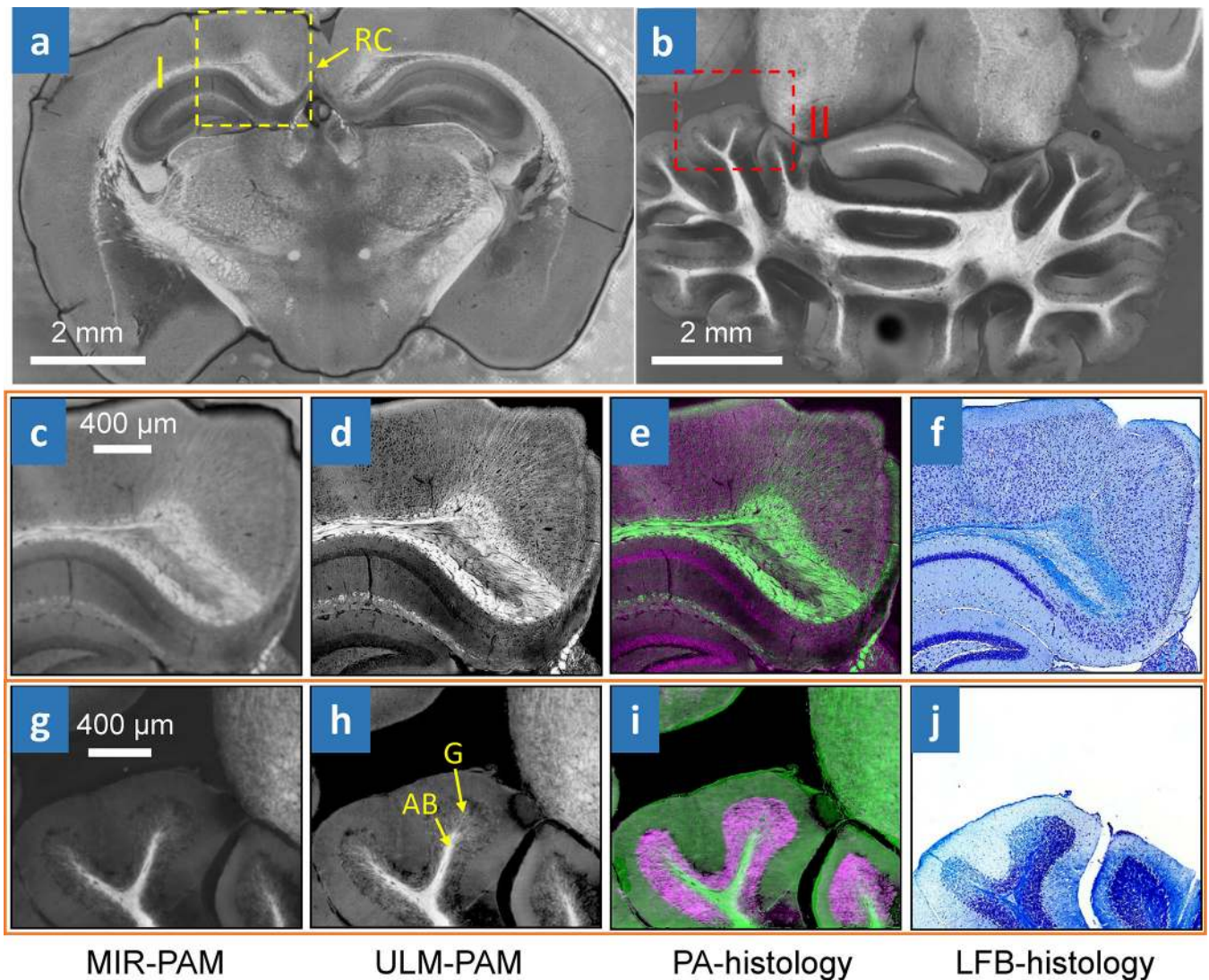
Figure 4.
Imaging of mouse brain slices. a, b. MIR-PAM images of myelin in 300 μm thick slices of (a) the cerebrum and (b) the cerebellum. RC, retrosplenial cortex. c. Close-up MIR-PAM image of myelin. d. ULM-PAM image of myelin. e. PA-histologic image. f. LFB-stained histologic image of the same area (I) shown in the cerebrum image (a). g. Close-up MIR-PAM image of myelin. h. ULM-PAM image of myelin. AB, arbor vitae region; G, granular region. i. PA histologic image. j. LFB-stained histologic image of the same area (II) shown in the cerebellum image (b). In the PA-histologic images, green represents myelin and violet represents nucleic acids. In the LFB-stained histologic images, blue represents myelin and deep blue represents nucleic acids.